



**HAL**  
open science

# Simulations of laser imprint reduction using underdense foams and its consequences on the hydrodynamic instability growth

M Olazabal-Loumé, Ph Nicolaï, G Riazuelo, M Grech, J Breil, S Fujioka, A Sunahara, N Borisenko, V T Tikhonchuk

## ► To cite this version:

M Olazabal-Loumé, Ph Nicolaï, G Riazuelo, M Grech, J Breil, et al.. Simulations of laser imprint reduction using underdense foams and its consequences on the hydrodynamic instability growth. *New Journal of Physics*, 2013, 15, pp.085033. 10.1088/1367-2630/15/8/085033 . hal-01587071

HAL Id: hal-01587071

<https://hal.sorbonne-universite.fr/hal-01587071>

Submitted on 13 Sep 2017

**HAL** is a multi-disciplinary open access archive for the deposit and dissemination of scientific research documents, whether they are published or not. The documents may come from teaching and research institutions in France or abroad, or from public or private research centers.

L'archive ouverte pluridisciplinaire **HAL**, est destinée au dépôt et à la diffusion de documents scientifiques de niveau recherche, publiés ou non, émanant des établissements d'enseignement et de recherche français ou étrangers, des laboratoires publics ou privés.



Distributed under a Creative Commons Attribution 4.0 International License



PAPER • OPEN ACCESS

## Simulations of laser imprint reduction using underdense foams and its consequences on the hydrodynamic instability growth

To cite this article: M Olazabal-Loumé *et al* 2013 *New J. Phys.* **15** 085033

View the [article online](#) for updates and enhancements.

### Related content

- [Physics issues for shock ignition](#)  
D. Batani, S. Baton, A. Casner et al.
- [Classical and ablative Richtmyer–Meshkov instability and other ICF-relevant plasma flows diagnosed with monochromatic x-ray imaging](#)  
Y Aglitskiy, M Karasik, A L Velikovich et al.
- [Linear and non-linear amplification of high-mode perturbations at the ablation front in HiPER targets](#)  
M Olazabal-Loumé, J Breil, L Hallo et al.

### Recent citations

- [Focus on high energy density physics](#)  
R Paul Drake and Peter Norreys

## Simulations of laser imprint reduction using underdense foams and its consequences on the hydrodynamic instability growth

M Olazabal-Loumé<sup>1,6</sup>, Ph Nicolai<sup>1</sup>, G Riazuelo<sup>2</sup>, M Grech<sup>3</sup>,  
J Breil<sup>1</sup>, S Fujioka<sup>4</sup>, A Sunahara<sup>4</sup>, N Borisenko<sup>5</sup>  
and V T Tikhonchuk<sup>1</sup>

<sup>1</sup> Université de Bordeaux, CEA, CNRS CELIA (Centre des Lasers Intenses et Applications), UMR 5107, F-33400 Talence, France

<sup>2</sup> CEA, DAM, DIF, F-91297 Arpajon, France

<sup>3</sup> LULI, Ecole Polytechnique, CNRS, CEA, UPMC, F-91128 Palaiseau, France

<sup>4</sup> Institute of Laser Engineering, Osaka University, Suita, Osaka 565, Japan

<sup>5</sup> P N Lebedev Physical Institute, RAS, 53 Leninskii Prospect, Moscow 119991, Russia

E-mail: [olazabal@celia.u-bordeaux1.fr](mailto:olazabal@celia.u-bordeaux1.fr)

*New Journal of Physics* **15** (2013) 085033 (19pp)

Received 7 March 2013

Published 28 August 2013

Online at <http://www.njp.org/>

doi:10.1088/1367-2630/15/8/085033

**Abstract.** The mechanisms of laser imprint reduction on a surface of a planar foil performed using an underdense foam are presented. The consequences on the Rayleigh–Taylor instability growth at the ablation front when the foil is accelerated are studied. The analysis is based on numerical simulations using a chain of codes: the electromagnetic paraxial code PARAX provides the modifications of the intensity perturbation spectrum while the laser beam is crossing the foam. Two-dimensional axially symmetric simulations with the radiation hydrodynamic code CHIC describe the foam expansion and the foil dynamics. Finally, the perturbed flow calculations and the instability growth are investigated with the two-dimensional CHIC version in the planar geometry

<sup>6</sup> Author to whom any correspondence should be addressed.



Content from this work may be used under the terms of the [Creative Commons Attribution 3.0 licence](http://creativecommons.org/licenses/by/3.0/). Any further distribution of this work must maintain attribution to the author(s) and the title of the work, journal citation and DOI.

by using the initial and smoothed perturbation spectra. The dominant role of temporal laser smoothing during the time of foam crossing by the laser beam is demonstrated. Applications to the direct drive targets for inertial confinement fusion are discussed.

## Contents

<b>1. Introduction</b>	<b>2</b>
<b>2. Hydrodynamic simulations of the macroscopic plasma dynamics: target heating and expansion</b>	<b>4</b>
<b>3. Plasma-induced laser-beam smoothing</b>	<b>6</b>
3.1. PARAX simulation setup . . . . .	6
3.2. Numerical results and characterization of the plasma-induced smoothing . . . . .	7
<b>4. Hydrodynamic simulations of the perturbed flow in the plastic foil</b>	<b>11</b>
4.1. Dynamics of the foil in single-mode simulations . . . . .	12
4.2. Simulations of the laser imprint multimode perturbation . . . . .	14
<b>5. Conclusion</b>	<b>17</b>
<b>Acknowledgments</b>	<b>18</b>
<b>References</b>	<b>18</b>

## 1. Introduction

Mitigation of hydrodynamic instability development is an important issue in the direct-drive inertial confinement fusion (ICF) [1, 2]. These instabilities are seeded by the initial perturbations of the target surface and/or by the laser intensity non-uniformities that are imprinting density modulations at the beginning of the laser irradiation. The Rayleigh–Taylor (RT) instability starts to grow later in time when the target is accelerated under the ablation pressure. To control the instability growth one can reduce either the initial perturbation amplitude or the instability growth rate by using dedicated target designs. Different versions of the RT instability control have been proposed. The adiabat shaping technique aims at the growth rate reduction by increasing the plasma ablation velocity. This can be achieved by using a target coating with high atomic number material [3], or applying a low [4, 5] or high intensity [6, 7] laser picket. One can also vary the plasma density profile in the RT unstable zone by increasing the role of radiative energy transport by using moderate atomic number ablator layers. This approach has been demonstrated experimentally [8, 9] and studied theoretically [10–12]. The laser imprint reduction takes place during the late time plasma expansion due to the increase of the conduction zone length. The electron thermal conductivity in the plasma corona is smoothing out the density perturbations with wavelengths larger than the density gradient scale length [5, 7]. Nevertheless, at the very early time, during the first nanosecond of laser target interaction, the plasma corona is very short and thermal smoothing cannot mitigate the laser imprint. Other methods of imprint reduction have to be used. The use of supercritical low density plastic foams have been studied several years ago [13]. The principle was to launch a supersonic wave in the foam by irradiating a thin layer of metal placed at the front side of the foam. This process

led to undesirable preheating due to the x-ray emission of this metallic layer. Subcritical low density foams could be an efficient solution for the early imprint reduction. They readily absorb the initial part of the laser pulse and produce an extended corona of a low density plasma. It is known since now several years [14, 15] that the laser beam propagation through a plasma with the electron density  $n_e$  much lower than the critical density  $n_c = \epsilon_0 m_e \omega_0^2 / e^2$  is accompanied by a loss of both spatial and temporal coherence of the laser beam<sup>7</sup>. This phenomenon, known as plasma-induced laser beam smoothing, arises from the forward scattering of the laser light on the plasma density perturbations induced by the laser itself. Several processes of plasma-induced laser beam smoothing have been identified: namely, the electromagnetic filamentation instability (FI) [15, 16], the stimulated Brillouin scattering in near forward direction (FSBS) [17–19], or laser multiple scattering on spontaneous density perturbations [20, 21]. The resulting reduction of the laser spatial coherence is associated with a reduced size of the laser speckles in the far field zone and with a widening of the laser aperture angle (so-called, beam spraying). The reduction of the laser beam temporal coherence is associated with a reduced lifetime of the speckles and the broadening of the laser frequency spectrum. Plasma induced smoothing leads to a more homogeneous laser energy deposition in the target and thus to a smaller amplitude of density perturbations in the ablation zone.

Experiment [22] confirmed the possibility of reducing such early imprinted perturbations by using copper foils covered by underdense plastic foams. Foams with thickness of a few hundred microns and density in the range 20–30% of the critical density were irradiated by a laser pulse with intensity of the order of  $100 \text{ TW cm}^{-2}$  and duration of a few ns. The laser imprint was measured thanks to the soft x-ray emission of a copper foil set at the rear side of the foam. This experiment was dedicated to studies of the plasma smoothing process. No measurements of the imprint reduction effect on the hydrodynamic instability growth were performed. The time integrated imaging of the foil x-ray emission showed that the foam modifies the initial spatial pattern by smearing out the large laser scale perturbations. The role of parametric instabilities in the laser beam smoothing by an underdense plasma has been confirmed in numerical simulations with the electromagnetic paraxial code PARAX [23]. The time dependence of the beam intensity pattern behind the foam leads to a lower imprinted perturbation amplitude associated with the spectrum shifted to shorter wavelengths. This effect we call ‘temporal smoothing’. More recently, measurements of foam crossing time were performed at the GEKKO XII facility and the foam homogenization was investigated [24]. Also, the smoothing effect was confirmed with paraxial numerical simulations [25].

Based on numerical simulations and theoretical considerations, the present work is dedicated to the modelling of the modification of the laser intensity distribution in an underdense plasma and its effect on the hydrodynamic evolution of a plastic foil placed at the rear side of the foam. The plasma-induced smoothing reduces significantly the amplitude and the wavelength of the perturbation, which evolution in the foil comprises two phases. Firstly, the shock is launched through the foil. The imprinted perturbation grows before oscillating [28]. These oscillations correspond to the ablative Richtmyer–Meshkov (RM) instability behaviour [26] that takes place during the shock transit time. They are due to the so-called stabilizing dynamic overpressure [27]. Secondly, after the shock is reflected from the rear target side, the foil is accelerated, and the ablative RT instability develops at the ablation front. By analysing the

<sup>7</sup> Here,  $\epsilon_0$  is the dielectric permittivity of vacuum,  $m_e$  and  $e$  are the electron mass and charge, and  $\omega_0$  is the frequency of the laser light.

sequence of these processes, we study the effect of the plasma-induced smoothing on the final state of the accelerated foil.

Section 2 presents the two-dimensional (2D) hydrodynamic simulations of the target evolution consisting of a low density plastic foam with a solid plastic foil behind. The density and temporal profiles of the plasma are extracted and used to initialize the laser propagation simulations in three spatial dimensions with a paraxial code. The results of paraxial simulations and the analysis of the spectrum of laser intensity fluctuations are presented in section 3. Section 4 is dedicated to the hydrodynamic simulations of the foil dynamics using the laser intensity pattern deduced from the paraxial simulations. 2D single-mode and multimode simulations are performed in order to discriminate the smoothing mechanism that has the most significant impact on the RT evolution. It is demonstrated that the dominant role is played by the laser beam temporal smoothing in the foam during the initial phase of the ablative RM instability, before the foil is accelerated as a whole. Our conclusions are presented in section 5.

## 2. Hydrodynamic simulations of the macroscopic plasma dynamics: target heating and expansion

Hydrodynamic simulations have been performed with the radiation hydrodynamic code CHIC [29] in 2D axially symmetric geometry. CHIC is a Lagrangian code dedicated to the design of inertial confinement fusion targets. It includes three-dimensional ray-tracing for laser beam propagation; the laser energy deposition is modelled by inverse bremsstrahlung absorption; the electron thermal transport is described in the classical Spitzer–Härm approximation with flux limitation, or with a non-local transport model. The equation of state is based on the SESAME or the QEOS tables and on the Thomas–Fermi model for ionization. A multigroup diffusion approximation of the radiation transport with the tabulated opacities is included in the code.

The baseline target is composed of a plastic foil set at the rear side of a  $500\ \mu\text{m}$  thick low density foam. The CH foil is made of carbon and hydrogen atoms with density  $1\ \text{g cc}^{-1}$  and thickness  $15\ \mu\text{m}$ . The foam is made of cellulose triacetate  $\text{C}_{15}\text{H}_{20}\text{O}_6$  with average density  $5\text{--}10\ \text{mg cc}^{-1}$  and for which the pore size is lower than  $1\ \mu\text{m}$ . This configuration corresponds to the experiment conducted in the target chamber II of the GEKKO XII laser facility [24]. The target is irradiated by a laser pulse at the wavelength of  $351\ \text{nm}$  with a maximum total power of  $150\ \text{GW}$ . The laser focal spot is described by a superposition of a super-Gaussian intensity profile of diameter  $100\ \mu\text{m}$  and low intensity wings. In the simulations the foam is modelled by a homogeneous material of an equivalent density. The foam homogenization can be accounted for with a temporal delay of the laser energy deposition as explained in [30]. However, this model is not used in the present simulations.

Figure 1 presents the temperature and pressure distributions at the moment when the ionization wave crosses the foam and the laser radiation approaches the CH foil. Due to the low foam density, the ionization wave propagates through the foam with a supersonic velocity. After  $100\ \text{ps}$ , the  $300\ \mu\text{m}$  thick foam layer has been ionized. This corresponds to a velocity of about  $3\ \mu\text{m ps}^{-1}$ , which is more than three times above the acoustic velocity. Thus, matter is ionized and heated before it starts to expand. The density remains almost constant behind the front. The temperature approaches  $1\ \text{keV}$  and the pressure just reaches  $2.2\ \text{Mbar}$ . No shock is created in the foam. After about  $150\ \text{ps}$ , the laser irradiates the solid plastic foil at the rear side of the foam, the foil is ionized by the laser and the ablation process begins. The foil is compressed

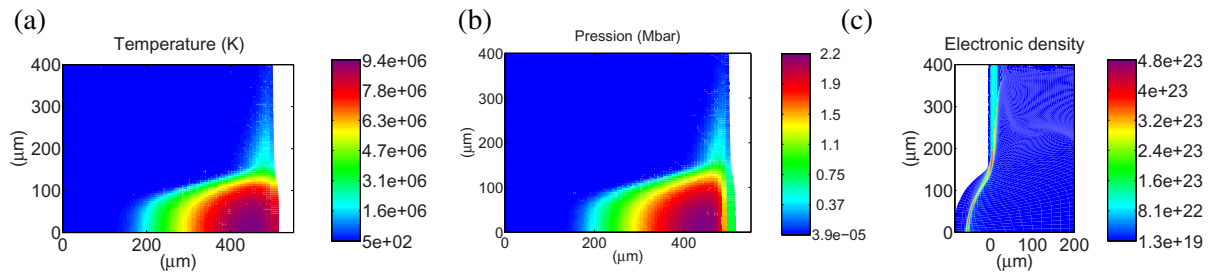


**Figure 1.** Isocontours of the temperature (a) and the pressure (b) during the time of foam ionization ( $t = 100$  ps). The foam thickness is  $500 \mu\text{m}$  and the density  $5 \text{ mg cc}^{-1}$ . (c) Isocontours of the electron density during the foil acceleration phase with foam. Laser comes from the right.

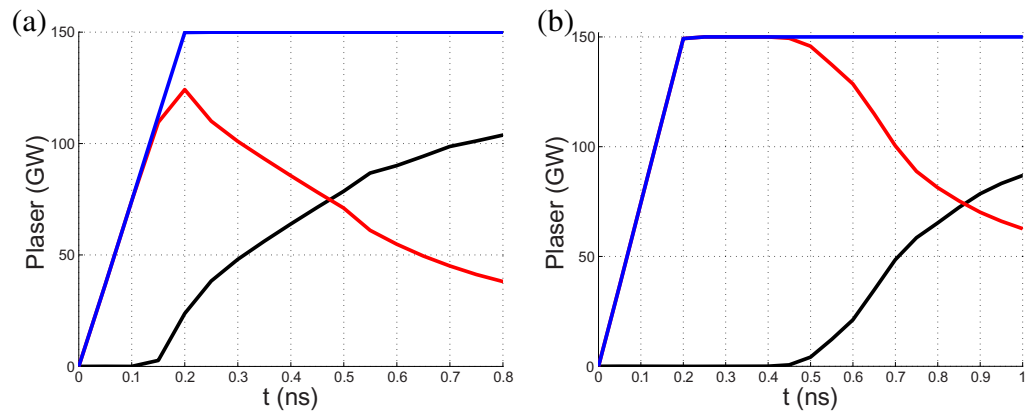


**Figure 2.** Temporal evolution of the laser pulse power (blue) and the fractions of absorbed laser power in the foam (red) and in the foil (black) for the foam average density  $5 \text{ mg cc}^{-1}$  (a) and  $10 \text{ mg cc}^{-1}$  (b).

by a shock and the rarefaction wave propagates backward through the foam. After the shock breaks out at the rear foil surface, the foil is accelerated.

Figure 1(c) shows the isocontours of the electron density during the acceleration phase at time 1 ns. The plastic foil is moving in the laser propagation direction. It is compressed and bended because of the inhomogeneous radial laser intensity distribution. As the shock has already crossed the foil, the rarefaction wave propagates backward. When the laser irradiates the CH foil, it takes between 250 and 300 ps for the shock wave to cross the foil. Then the acceleration of the central part of the foil is of the order  $300 \mu\text{m ns}^{-2}$ .

At the beginning of the acceleration phase, the foam plasma continues to absorb the laser energy. Figure 2 shows the time dependence of the laser power and the power absorbed in the foam and in the foil. The absorption in the foam begins when the ionization wave crosses the foam. Then the part of energy absorbed in the foam decreases due to its expansion. About 70% of the laser power is absorbed in the foil when it is accelerated. These 2D simulations provide the hydrodynamic profiles that are used in the laser propagation simulations presented in the next

section. As the perpendicular size of the simulation box in the paraxial simulations is smaller than the laser beam radius, the plasma is assumed to be initially homogeneous in the transverse direction and the longitudinal profiles are taken along the central position. This approach is consistent with recent experimental results [24].

### 3. Plasma-induced laser-beam smoothing

The simulations of the plasma-induced laser-beam smoothing have been performed with the massively parallel code PARAX [17, 23, 31] that describes the laser beam propagation in the paraxial approximation in three spatial directions. The aim was to characterize the foam plasma effect on the laser intensity distribution.

#### 3.1. PARAX simulation setup

The laser propagation is described by considering the spatio-temporal evolution of the laser electric field envelope  $E$  slowly varying in space and time with respect to the laser period and wavelength. The paraxial approximation includes the corrections for light scattering at large angles. The laser propagation is affected by the laser-induced density fluctuations. The plasma evolution is described by a linearized hydrodynamic equation in the plane  $x, y$  perpendicular to the laser propagation direction,  $z$ . The laser radiation is accounted for using an ion-acoustic wave equation for the plasma density with the source terms describing both the ponderomotive force and electron heating [17]. In this context, the foam plasma is treated as a quasi-neutral fluid with constant and homogeneous (in the  $x, y$  plane) electron and ion temperatures, and laser-driven density fluctuations are assumed to be small:  $\delta n_e/n_e \ll 1$ . Furthermore, as the electron mean-free-path is, under the conditions relevant for this study, of the order of the characteristic laser speckle radius, nonlocal electron transport is accounted for according to the model by Brantov *et al* [32].

PARAX enables a full-scale multi-speckle simulation of the laser–plasma interaction. We consider here a propagation of the whole laser beam, with an initial circular cross section described by a sixth order super-Gaussian transverse intensity distribution with  $200 \mu\text{m}$  full-width at half-maximum (FWHM) and a constant in time average intensity  $I_0 \simeq 500 \text{ TW cm}^{-2}$ . The speckle pattern at the plasma entrance is obtained as a numerical realization of a random-phase-plate [33]. The initial speckle transverse size (FWHM) is  $r_{\text{sp}} \simeq \lambda_0 f_{\#} \sim 2.85 \mu\text{m}$ , where  $f_{\#} = 7.8$  is the laser-beam aperture, and  $\lambda_0 = 0.351 \mu\text{m}$  is the laser wavelength. The simulated volume is  $500\text{--}1000 \mu\text{m}$  in the parallel direction and  $300 \mu\text{m}$  in the perpendicular directions. No additional (optical) temporal smoothing technique is considered here.

To investigate the effect of the foam plasma on the laser propagation, two plasma densities,  $5$  and  $10 \text{ mg cc}^{-1}$ , have been considered in our simulations. The PARAX simulations are initialized using the density and temperatures profiles obtained from the CHIC hydrodynamic simulations presented in section 2 at a given time  $t_0$ . The paraxial simulations are then run for the time  $t_s = 50 \text{ ps}$ , which is long enough for the parametric instabilities responsible for the plasma-induced laser beam smoothing to develop, and short enough to neglect the overall hydrodynamic expansion of the foam plasma. To account for the effect of the foam expansion, two different initialization times  $t_0$  have been considered for each foam.

### 3.2. Numerical results and characterization of the plasma-induced smoothing

3.2.1. *Reduction of the laser spatial coherence and speckle size.* Spatial laser beam smoothing is characterized by the reduction of the laser spatial coherence. It is identified in our simulations by the laser electric field correlation function

$$\Gamma_s(t, z, \mathbf{r}) = \left\langle E \left( t, z, \mathbf{R} + \frac{\mathbf{r}}{2} \right) E^* \left( t, z, \mathbf{R} - \frac{\mathbf{r}}{2} \right) \right\rangle_{\mathbf{R}}, \quad (1)$$

where  $\mathbf{R}$  and  $\mathbf{r}$  lie in the plane  $(x, y)$  transverse to the laser propagation direction. While the angular brackets in (1) denote the statistical average over the possible speckle pattern realizations, in practice, this averaging is approximated by a spatial averaging over a region that contains a sufficiently large number of speckles [21]. The profiles of the square-modulus of the spatial correlation functions along the propagation through the foam plasma are shown in figure 3(a) for the case of a  $5 \text{ mg cc}^{-1}$  foam, at time  $t_0 + t_s$  with  $t_0 = 500 \text{ ps}$ . As the laser propagates through the plasma, the correlation function gets narrower: the spatial coherence of the laser beam is reduced. The coherence radius of the laser light is henceforth defined as the FWHM of the square-modulus of this spatial correlation function. As can be seen in figure 3(b), this coherence radius  $r_{\text{coh}}$  decreases with the propagation distance through the plasma from  $\sim 2.85 \mu\text{m}$  at the beginning of the plasma to  $\sim 1.0\text{--}1.3 \mu\text{m}$  after a few hundred microns of propagation.

This reduction of the coherence radius of the laser light is due to the plasma-induced spatial smoothing. It is associated with the reduction of the characteristic radius of the speckles in the focal spot. This can be observed in figure 3(c) where the average speckle radius  $r_{\text{sp}}$  is presented as a function of the propagation distance through the plasma. It was calculated by using a specific diagnostic tool, which detects individually each speckle in a transverse plane and computes its width, power and the distribution of intensity [34]. Here again,  $r_{\text{sp}}$  is found to decrease from  $\sim 3 \mu\text{m}$  at the entrance of the plasma to  $\sim 1.0\text{--}1.5 \mu\text{m}$  after propagation through the whole plasma. For optically randomized laser beams with a Gaussian statistics, the intensity variation near a hot spot is described by  $|\Gamma_s|^2$  [35]. This is why the two diagnostics in figures 3(b) and (c) give very similar results.

Due to the reduction of the speckle radius, plasma-induced laser beam smoothing is associated with an increase of the laser beam angular aperture by a factor varying from 2.2 to 3 in our simulations. This increased divergence of the laser light (see also figure 3(d)), or beam spraying, results in a decreased laser intensity incident on the foil one wishes to accelerate. This effect is however, under current conditions, negligible compared to the laser intensity reduction due to laser absorption in the foam plasma.

3.2.2. *Reduction of the laser temporal coherence and time-integrated contrast.* In addition to induced spatial incoherence, the propagation of a randomized laser beam through the plasma induces a temporal incoherence in the transmitted laser light. This temporal smoothing can be identified in our simulations by calculating the temporal correlation function of the laser electric field. In PARAX, this correlation function is reconstructed from the laser light spectrum  $\langle |E(\omega, z, \mathbf{R})|^2 \rangle_{\mathbf{R}}$  by the inverse Fourier transform

$$\Gamma_t(z, \tau) = \int d\omega \langle |E(\omega, z, \mathbf{R})|^2 \rangle_{\mathbf{R}} \exp(i\omega\tau), \quad (2)$$

where the averaging is here again made in the plane  $x, y$  containing many speckles. The square-modulus of the correlation function is presented for different propagation distances

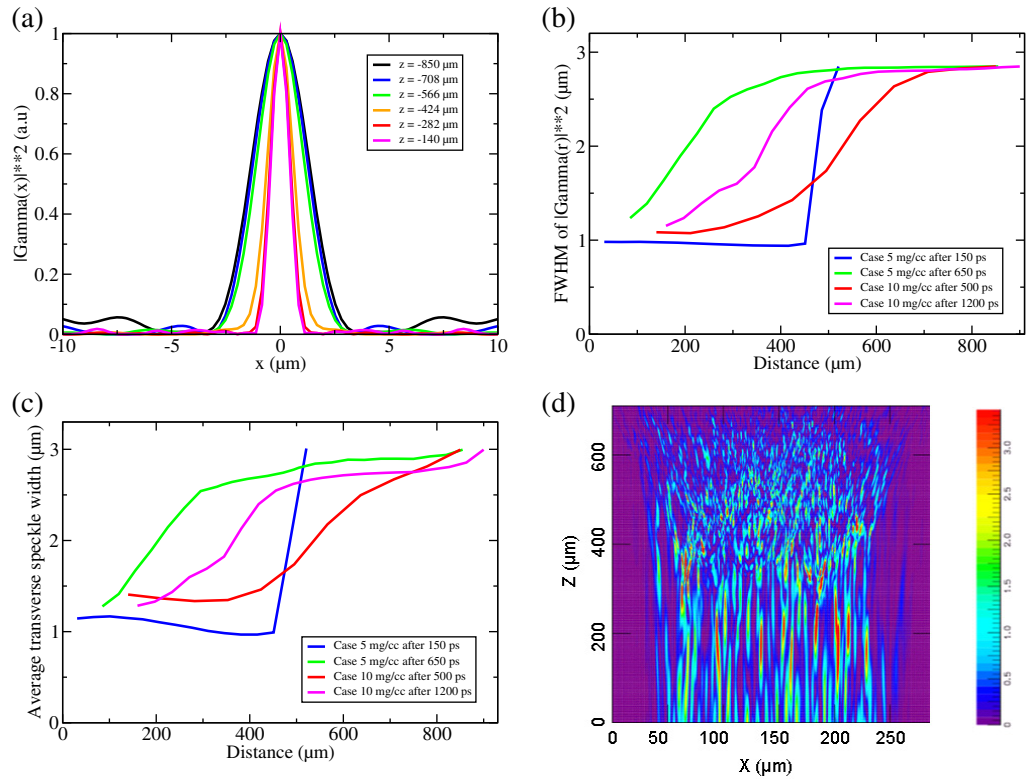


**Figure 3.** (a) Square modulus of the spatial correlation function of the laser electric field for different position along the plasma (from black to magenta as  $z$  increases) every  $140 \mu\text{m}$ ) at time  $t_0 + t_s$ , for the case of a  $10 \text{ mg cc}^{-1}$  foam and  $t_0 = 500 \text{ ps}$ . The normalization is chosen so that the maximum of the square-modulus equals unity. (b) Evolution along the laser propagation direction of the laser coherence radius  $r_{\text{coh}}$  defined as the FWHM of the square-modulus of the spatial correlation function taken at the end of the simulation,  $t = t_0 + t_s$ . For the  $5 \text{ mg cc}^{-1}$  foam with  $t_0 = 150 \text{ ps}$  (blue curve) and  $t_0 = 650 \text{ ps}$  (green curve). For the  $10 \text{ mg cc}^{-1}$  foam with  $t_0 = 500 \text{ ps}$  (red curve) and  $t_0 = 1200 \text{ ps}$  (magenta curve). (c) Evolution along the laser propagation direction of the average speckle radius calculated as the average FWHM of the intensity variation around local maxima. Parameters and colour code are the same as for panel (b). (d) Intensity distribution in the  $z$ ,  $x$  plane at the end of the simulation,  $t = t_0 + t_s$ , for the case depicted in panel (a).

in figure 4(a). As no optical temporal smoothing is considered in this study, at the entrance of the plasma, the temporal correlation function is constant over a time corresponding to the laser pulse duration (here equal to the duration of the simulation). As the laser propagates deeper into the plasma, the temporal correlation function gets narrower. The laser beam coherence time  $\tau_{\text{coh}}$ , henceforth defined as the FWHM of the square-modulus of the temporal correlation function, decreases down to typically  $\tau_{\text{coh}} \sim 1 \text{ ps}$  as it can be seen in figure 4(b).

It is important to note that the dominating role of the near-forward Brillouin scattering (FSBS) on the induced laser beam smoothing can be readily identified when investigating the

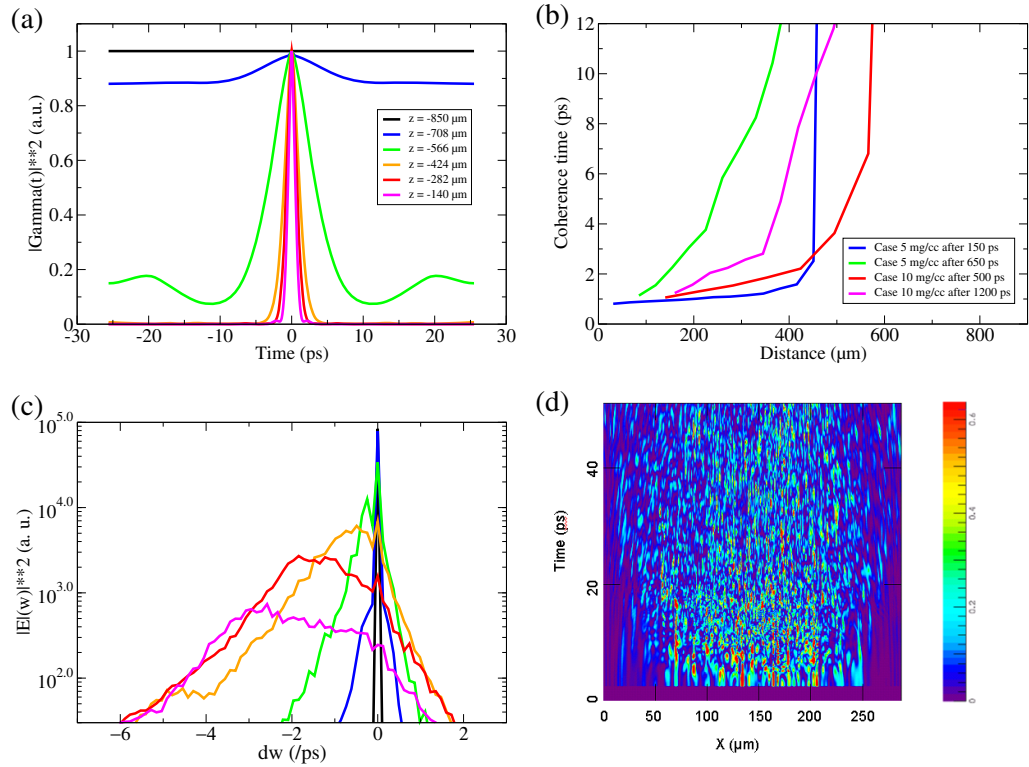


**Figure 4.** (a) Square modulus of the temporal correlation function of the laser electric field at the different positions along the plasma (from black to magenta as  $z$  increases) at time  $t_0 + t_s$ , for the case of a  $10 \text{ mg cc}^{-1}$  foam and  $t_0 = 500 \text{ ps}$  (same conditions as in figure 3(a)). The normalization is chosen so that the maximum of the square-modulus equals unity. (b) Evolution along the laser propagation direction of the laser coherence time  $\tau_{\text{coh}}$  defined as the FWHM of the square-modulus of the temporal correlation function taken at the end of the simulation  $t = t_0 + t_s$ . For the  $5 \text{ mg cc}^{-1}$  foam with  $t_0 = 150 \text{ ps}$  (blue curve), and  $t_0 = 650 \text{ ps}$  (green curve). For the  $10 \text{ mg cc}^{-1}$  foam with  $t_0 = 500 \text{ ps}$  (red curve), and  $t_0 = 1200 \text{ ps}$  (magenta curve). (c) Laser spectrum centred on the laser main wavelength  $\lambda_0 = 2\pi c/\omega_0$  for different positions in the plasma. Same conditions and the colour code as in panel (a). (d) Temporal evolution of the transverse (along the  $x$ -axis) intensity distribution after propagation through the whole plasma. Same conditions as for panel (a).

spatial evolution of the laser light temporal spectrum. Figure 4(c) shows this spectrum (averaged over the beam transverse size) for the case of a  $5 \text{ mg cc}^{-1}$  foam at time  $t_0 + t_s$  with  $t_0 = 500 \text{ ps}$ . At the plasma entrance, the temporally coherent laser beam has a narrow,  $\delta$ -function-like spectrum centred at the beam main wavelength  $\Delta\lambda = 0$ . As the beam propagates through the plasma, one observes: (i) a reduction of the signal at  $\Delta\lambda = 0$  (due to the depletion of the laser beam due to FSBS), and both (ii) a widening of the spectrum (denoting the loss of temporal coherence of the laser light) and (iii) an overall shift of the spectrum to longer wavelengths characteristic for FSBS [15, 19].

The speckles in a temporally incoherent laser beam are moving in the plasma. The resulting time-dependence of the randomized intensity distribution can be clearly observed in figure 4(d), where the transverse intensity distribution after propagation through the whole plasma is shown as a function of time for the case of a  $10 \text{ mg cc}^{-1}$  foam and  $t_0 = 500 \text{ ps}$ . The characteristic lifetime of the speckles is close to the laser light coherence time presented in figure 4(b). As a result, the homogeneity of the foil irradiation is improved. The contrast of the time-averaged laser intensity distribution, defined as

$$C = \sqrt{\langle I^2 \rangle / \langle I \rangle^2 - 1}, \quad (3)$$

where the angular brackets denote an average over both the transverse  $x, y$ -plane and time. It is reduced from the initial value of 1 to  $C = 0.25$ . In next section, we will see that this homogenized irradiation helps in reducing the hydrodynamic instability seeding.

*3.2.3. Two interaction regimes.* In both simulations corresponding to the foam average densities 5 and  $10 \text{ mg cc}^{-1}$  the efficient spatio-temporal smoothing of the laser beam is mainly due to the FSBS instability. Indeed the PARAX simulations indicate a very similar evolution of the coherence radius and the coherence time with the propagation distance through the plasma for both simulations for  $t_0 = 650 \text{ ps}$ . However, the case of the lowest foam density with  $t_0 = 150 \text{ ps}$  stands apart. In this latter case, one observes a sudden (over a few tens of microns) reduction of the spatial and temporal coherence of the laser light. This sudden reduction, which occurs on a distance smaller than the characteristic speckle Rayleigh length  $\propto k_0 r_{\text{coh}}^2 \sim 130 \mu\text{m}$ , is a clear signature of the FI. It develops when a significant number of speckles carry a power larger than the critical power for the ponderomotive self-focusing [36]:

$$P_c \simeq 32 \text{ MW} \times \frac{T_e + 3 T_i / Z}{n_e / n_c}, \quad (4)$$

where the electron ( $T_e$ ) and ion ( $T_i$ ) temperatures are in keV, and  $Z = 3.85$  is the average ion charge-state in our foam plasma. For this particular case of a  $5 \text{ mg cc}^{-1}$  foam with  $t_0 = 150 \text{ ps}$ , the hydrodynamic simulations indicate that the foam plasma is already fully ionized, but is not yet expanding. The resulting electron density is therefore quite large,  $n_e \sim 0.17 n_c$ , while the average electron and ion temperatures are quite low:  $T_e \sim 0.8 \text{ keV}$  and  $T_i \sim 0.25 \text{ keV}$ , respectively. One thus obtains the critical power  $P_c \simeq 185 \text{ MW}$ .

Moreover, under the conditions of this simulation and for weakly collisional plasmas, thermal effects lead to an enhancement of the plasma response, which results in a reduction of the critical power by a factor  $\eta \simeq 1 + 1.66 \bar{Z}^{5/7} (r_{\text{sp}} / \lambda_{\text{ei}})^{(4/7)}$ , where  $\bar{Z} = \langle Z^2 \rangle / Z \simeq 5.3$  [32]. Under such conditions, the electron mean free path  $\lambda_{\text{ei}} \simeq 2.5 \mu\text{m}$  and thus  $\eta \simeq 6.8$ . Consequently, the FI threshold,  $P_{\text{th}} = P_c / \eta \simeq 30 \text{ MW}$ .

In comparison, for this particular simulation, the power in a speckle at the average intensity is, at the entrance of the plasma,  $P_{\text{sp}} \simeq 45 r_{\text{sp}}^2 \langle I \rangle \text{ MW}$ . One thus obtains that, for this particular configuration,  $P_{\text{sp}} \gtrsim P_c / \eta$ . Laser-plasma interaction under such conditions is therefore propitious for the FI to develop [15].

In contrast, for the three other simulations, the ratio  $\eta P_{\text{sp}} / P_c$  does not exceed 0.3 and plasma-induced smoothing is dominated by FSBS. This collective effect, which develops over several speckle lengths [19], gives rise to a more gentle reduction of the laser coherence properties.

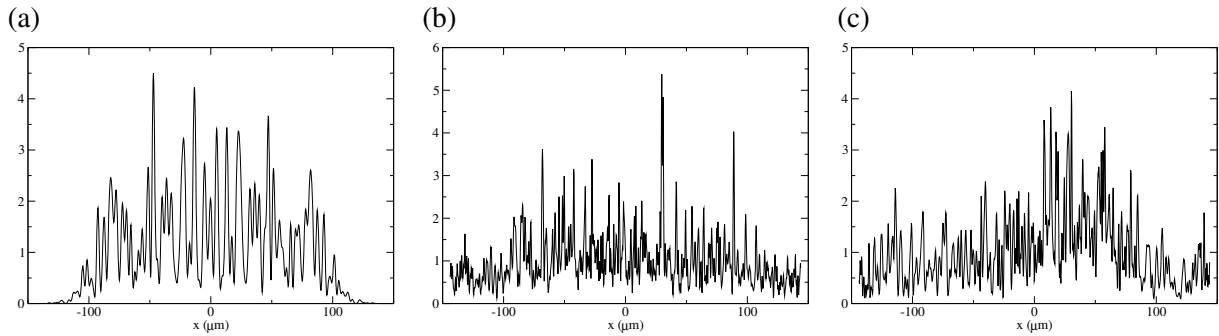


**Figure 5.** (a) Realization of the incident laser speckle pattern  $I(x)/I_0$  for the characteristic speckle size of  $3 \mu\text{m}$  and  $\epsilon = 1$ . Instantaneous laser speckle pattern obtained in PARAX simulations after crossing  $500 \mu\text{m}$  plasma made of  $5 \text{ mg cc}^{-1}$  foam (b) and  $10 \text{ mg cc}^{-1}$  foam (c).

**3.2.4. Laser intensity correlation function.** The hydrodynamic stability of the plastic foil in the next section is studied by applying a modulated laser intensity distribution at the front foil surface. According to the results of paraxial simulations reported above, the perturbed intensity distribution in the planar 2D geometry used in the next section is presented in the form

$$I(t, x) = I_t \left[ 1 + \epsilon \int dk (C(t, k) \cos(kx) + S(t, k) \sin(kx)) \right]. \quad (5)$$

Here  $I_t$  is the average laser intensity transmitted through the foam, the functions  $C$  and  $S$  present the normalized spectrum of the intensity perturbations at the front foil surface and  $\epsilon$  is a parameter in the range  $[0, 1]$ . These functions were produced with a Monte Carlo generator providing the statistical pattern corresponding to the Gaussian distribution of the perturbations according to the method described in [37]. The perturbation amplitude, central wave number and the spectral width were taken according to the paraxial simulations presented above in this section. Figure 5(a) shows a typical realization of the laser intensity pattern in the focal spot corresponding to the characteristic speckle size of  $3 \mu\text{m}$ .

Modifications of the laser intensity speckle pattern presented in figure 5(a) after crossing the foam plasma are shown in panels (b) and (c) of figure 5. The coherence length is reduced to  $1 \mu\text{m}$  while the contrast remains approximately on the same level. This is due to the fact that the distributions shown in figure 5 correspond to the instantaneous realization and do not account for the temporal smoothing. The square of the intensity norm is proportional to  $C(k)^2 + S(k)^2$  (from equation (5)) which is presented in figure 6 for the three examples shown in figure 5. Two effects characteristic of the laser induced smoothing can be noted: firstly, the spectrum envelope decreases in amplitude by a factor 2 or 3; secondly, the spectrum is broadened and modes with higher spatial frequencies appear. As it will be discussed in the next section, the range of wave numbers of particular importance for seeding of the RT instability corresponds to  $k \sim 0.01\text{--}0.03 \omega_0/c$ , correspondingly to wavelengths of  $10\text{--}30 \mu\text{m}$ .

#### 4. Hydrodynamic simulations of the perturbed flow in the plastic foil

In this section, we study the 2D hydrodynamic response of the CH foil to the inhomogeneous intensity irradiation and focus our attention on the development of hydrodynamic instabilities.

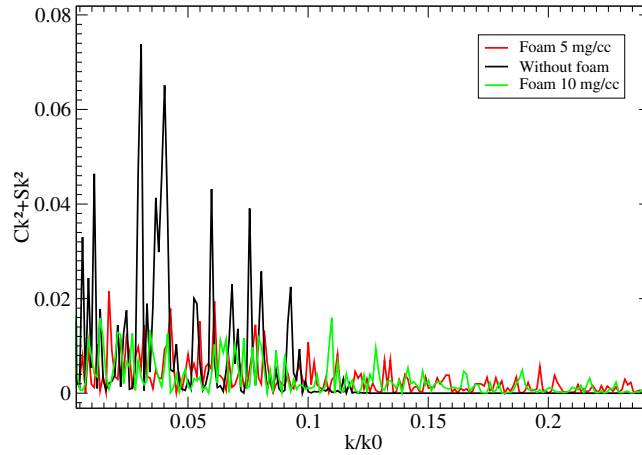


**Figure 6.**  $C(k)^2 + S(k)^2$  value for the incident laser beam (black) and after crossing a foam layer of  $500 \mu\text{m}$  of a density  $5 \text{ mg cc}^{-1}$  (red) and  $10 \text{ mg cc}^{-1}$  (green). The mode number is normalized by the laser wave number  $k_0 = \omega_0/c$ .

Hydrodynamic simulations of the CH foil evolution under the modulated laser intensity (5) were performed with the code CHIC in a 2D planar geometry. The foam plasma was not included in these simulations. The laser intensity distribution (5) was injected directly in the energy deposition term via the electron energy conservation equation. Although the interaction of the foam and the foil plasmas may modify the foil dynamics and affect the laser energy absorption, here the goal is to make clear comparisons of the perturbation evolution by modifying only the spectrum of the laser intensity with the same average values.

In what follows, we discuss two simulation setups. First, in section 4.1 we present single-mode simulations for a harmonic intensity perturbation with a given wavenumber  $k = 2\pi/\lambda$  corresponding to the characteristic scale  $\lambda$  of the laser intensity perturbations. This allows us to evaluate the instability growth rate and to compare it with theoretical estimates. Then, multi-mode simulations are discussed in section 4.2. For these simulations, the functions  $C(t, k)$  and  $S(t, k)$  enable us to reconstruct laser intensity distributions similar to the speckle pattern obtained in the PARAX simulations.

The foil section simulated here represents the central part of the CH foil with the transverse size less than  $100 \mu\text{m}$ , smaller than the laser spot size. Consequently, we extracted from the original full-scale axisymmetric simulations the equivalent one-dimensional (1D) planar flow dynamics occurring on the laser beam axis.

#### 4.1. Dynamics of the foil in single-mode simulations

In single-mode simulations the laser intensity distribution at the foil surface is modelled according to equation (5) with  $C(t, k) = \delta(k - k_m)$  and  $S(t, k) = 0$ . The foil acceleration leads to the development of the ablative RT instability. The amplitude of the surface perturbation increases as  $a(t) = a_0 \exp(\gamma t)$ , where  $\gamma$  is the linear growth rate and  $a_0$  is the perturbation amplitude at the beginning of acceleration. Figure 7(a) presents the growth rates evaluated from CHIC single-mode simulations with very low initial perturbation amplitudes corresponding  $\epsilon = 1\%$  in (5), where  $\epsilon$  is the amplitude of the intensity perturbation normalized to the average

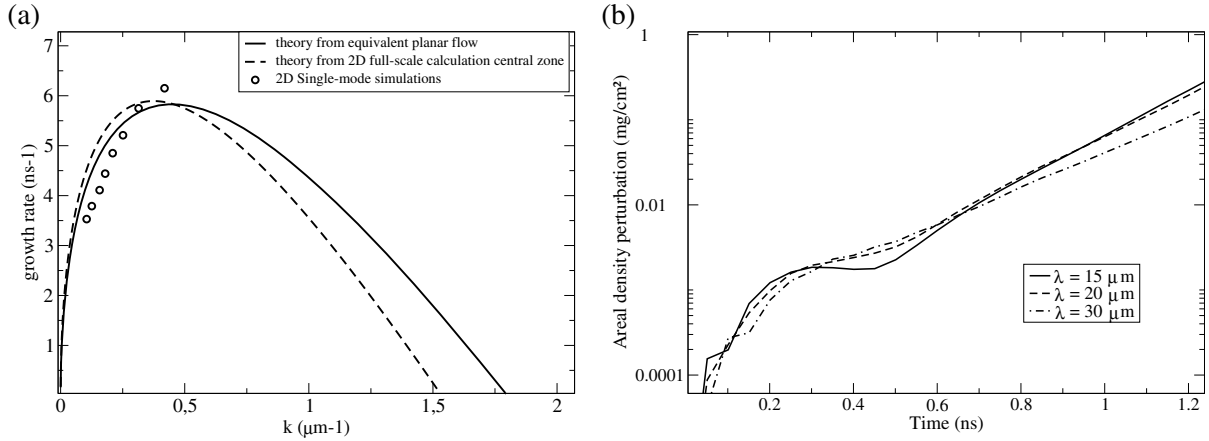


**Figure 7.** (a) RT instability linear growth rate at the ablation front obtained in 2D single-mode simulations (open circles) and the interpolations obtained with the modified Takabe formula (6) by using the parameters from the one-dimensional (1D) flow (solid line) and from the central part of the 2D flow (dashed line). (b) Temporal evolution of the areal density perturbation for wavelengths of 15, 20 and 30  $\mu\text{m}$  and the laser intensity modulation is  $\epsilon = 1\%$ .

intensity as defined in (5). Simulations correspond to the perturbation wavelengths varying from 15 to 60  $\mu\text{m}$ . The growth rates are estimated with the time-averaged (in the range 0.6–1 ns) values for the hydrodynamic flow. Calculated growth rates are fitted with the linear theory of the ablative RT instability [38] described by the modified Takabe formula

$$\gamma(k) = \alpha \sqrt{kg/(1+kL_{\min})} - \beta k V_a, \quad (6)$$

where  $g$  is the foil acceleration,  $V_a$  is the ablation velocity and  $L_{\min}$  is the averaged minimum density gradient length in the ablation zone. Fitting coefficients are  $\alpha = 1$  and  $\beta = 1.5$ . In the full-scale 2D simulations, we obtain the acceleration  $g \simeq 300 \mu\text{m ns}^{-2}$ , the ablation velocity  $5.8 \mu\text{m ns}^{-1}$  and the density gradient length of  $1.0 \mu\text{m}$  at the center of the target. To investigate the growth of hydrodynamic instabilities, we now consider an equivalent 1D planar flow with similar properties:  $g \simeq 260 \mu\text{m ns}^{-2}$ ,  $V_a \simeq 5.3 \mu\text{m ns}^{-1}$  and  $L_{\min} = 0.7 \mu\text{m}$ .

Hydrodynamic simulations show that the RT instability develops in the conditions of a low Froude number, which is a standard situation when a plastic ablator is used in direct-drive ICF designs. Single-mode calculations in the linear phase associated to the corresponding linear theory give an indication of the maximum growth rate range (here for 15–20  $\mu\text{m}$  perturbation wavelengths) and of the cut-off wave number. For our conditions the cut-off wavelength is found around  $\lambda_c \simeq 3.5 \mu\text{m}$ . Moreover, as shown in section 3, the plasma smoothing moves the characteristic speckle size even farther from the cut-off wavelength. Therefore, the long wavelength part of the laser intensity fluctuations is the most important for seeding the RT instability, and the largest size speckles dominate the imprint. The average speckle size reduction in a foam plasma does not contribute directly to the instability mitigation. A deeper analysis is needed to understand how the plasma smoothing modifies the probability of formation of large size speckles and what are the consequences on hydrodynamic flows.

The RT instability corresponds to the modulation of the target thickness. Thus, the growth rate can be extracted from the temporal evolution of the modulation of the target areal

density. Figure 7(b) shows the evolution of the areal density perturbation for the wavelength of 15 and 20  $\mu\text{m}$  (corresponding to the maximum growth rate) and 30  $\mu\text{m}$ . For the chosen initial conditions, the imprinted perturbation corresponds to an initial modulation of the order of  $10^{-4} \text{ mg cm}^{-2}$  at time  $t = 50 \text{ ps}$ .

During the shock transit time, the surface perturbation evolves due to the ablative RM instability. The imprinted perturbation amplitude first increases with time and then is submitted to oscillations. This phase corresponds to the first 0.4 ns of the evolution shown in figure 7(b). As the oscillation frequency increases when the perturbation wavelength decreases, the amplitude  $a_0$  at the beginning of acceleration phase depends on the perturbation wavelength. If the acceleration begins at the moment when the perturbation corresponds to a bump of the RM oscillation, the default starts to grow immediately. This is the case of the 20 and 30  $\mu\text{m}$  wavelengths in figure 7(b). In contrast, if at this moment the RM oscillation is in the valley phase, the perturbation growth is delayed. This is the case of the 15  $\mu\text{m}$  wavelength. The perturbation level reached by a given wavelength due to the ablative RT instability in the linear regime depends only on its own initial amplitude  $a_0$  and its growth rate  $\gamma$ . Although the 30  $\mu\text{m}$  perturbation starts from a higher amplitude, its level at  $t = 1.2 \text{ ns}$  is lower because of a smaller growth rate.

Single-mode simulations demonstrate a complicated interplay between the RM and RT phases, that depends on the irradiation temporal phase and on the perturbation wavelength. For instance, even if  $a_0$  is smaller for a 15  $\mu\text{m}$  perturbation, its RT growth rate is larger and produces a higher areal density perturbation level during acceleration. Thus, the dominant perturbation mode changes with time. As a consequence, multi-mode simulations are needed to describe the evolution of an initial laser imprint perturbation including the RM and RT phases, as well as mode coupling in the nonlinear regime.

## 4.2. Simulations of the laser imprint multimode perturbation

*4.2.1. Foil evolution under the pressure of a spatially incoherent laser beam.* The laser intensity distribution was initiated according to equation (5) with the stochastic functions  $C$  and  $S$  corresponding to the Gaussian process with the typical speckle size of 3  $\mu\text{m}$ . A realization of the laser intensity distribution in the focal plane before the foam is shown in figure 5(a). As explained in section 3, this is a static distribution corresponding to an infinite coherence time. As we are interested in the perturbation evolution in the central part of the foil, we simulate only a 40  $\mu\text{m}$  wide section of the foil (the central part of the distribution in figure 5) making sure that the intensity realization is representative in this zone. Figure 8 shows the foil density distributions obtained in the simulations during the acceleration time. The imprinted multimode perturbation develops at the ablation front close to the density maximum.

The perturbation evolution depends on the initial imprint level. When decreasing  $\epsilon$  from 60 to 5%, the time needed to reach approximately the same level and shape of the perturbation (corresponding here to the weakly nonlinear regime) increases from 700 ps to 1 ns. This can be readily understood as, here, only the initial perturbation level is modified but not the RT growth rate that depends on the global (large scale) hydrodynamic conditions, and thus on the average laser intensity. There is one-to-one relation between the intensity perturbation level  $\epsilon$  and the perturbation amplitude reached during the RT development. Therefore, in the following we consider  $\epsilon = 5\%$  as the reference case for further studies of the RT evolution in the nonlinear regime.

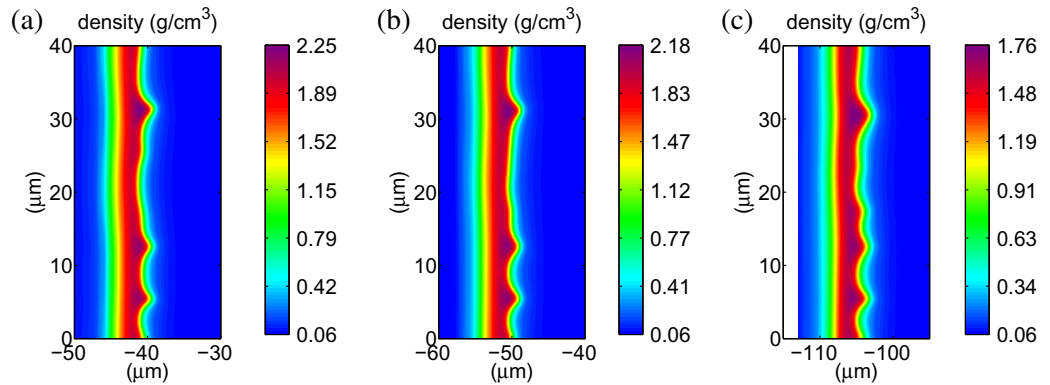


**Figure 8.** Isocontours of the foil density distribution during the acceleration phase for the case of a direct laser irradiation without foam, for the perturbation level  $\epsilon = 60\%$  (a),  $30\%$  (b) and  $5\%$  (c). The same amplitude and shape of the perturbation is achieved at times 700, 750 and 1000 ps for the three respective values of  $\epsilon$ . The laser beam arrives from the right.

Panels (a) and (b) in figure 9 present the foil density distributions at times 1 and 1.2 ns showing the stage of nonlinear RT evolution. Comparing these two figures, we observe more merging of perturbations at different wavelengths and the development of multimode bubble-spike structures. Thus, in the case of ablative RT, for a given wavelength  $\lambda$ , the nonlinear evolution begins for the amplitudes smaller than the standard criterion for the classical RT instability,  $a \sim 0.1 \lambda$  as shown in [39].

*4.2.2. Foil evolution under the smoothed laser irradiation conditions.* According to the paraxial simulations described in section 3, laser–plasma smoothing makes three distinct effects on the laser intensity pattern: (i) it decreases the characteristic wavelength, (ii) it decreases the coherence time and (iii) it decreases the time-integrated contrast. The speckle patterns corresponding to the spatially smoothed laser beam are presented in figure 5. The characteristic speckle size at the foam plasma exit is of the order of  $1 \mu\text{m}$ . Correspondingly, the level of intensity fluctuations in the long wavelength range decreases. This can be seen in figure 6. The effect of plasma smoothing on the ablation RT instability development is presented in figure 9. Panels (c) and (d) correspond to the case of a large coherence time, which is not realistic but allows to make a clear distinction between the role of the spatial and temporal effects.

One can barely see a difference from the density distributions in panels (a) and (b) obtained without the foam. Even if the envelope spectrum is globally reduced after crossing the foam, it still contains a significant contribution in the wavelength range of  $15\text{--}20 \mu\text{m}$  where the RT growth rate is sufficiently large. The smaller wavelengths created by the laser induced smoothing are too short to be amplified by the RT instability and thus do not contribute directly to the perturbation evolution. Thus, the spatial smoothing alone does not contribute to any noticeable mitigation of the large scale hydrodynamic instabilities.

Panels (e) and (f) in figure 9 present the foil density distributions obtained in the case where the temporal smoothing is taken into account in the laser intensity distribution. By using the coherence time  $\tau_{\text{coh}} = 1 \text{ ps}$  obtained from PARAX simulations, we found that the integrated intensity contrast is strongly reduced to the level 25%. Correspondingly, the density perturbation

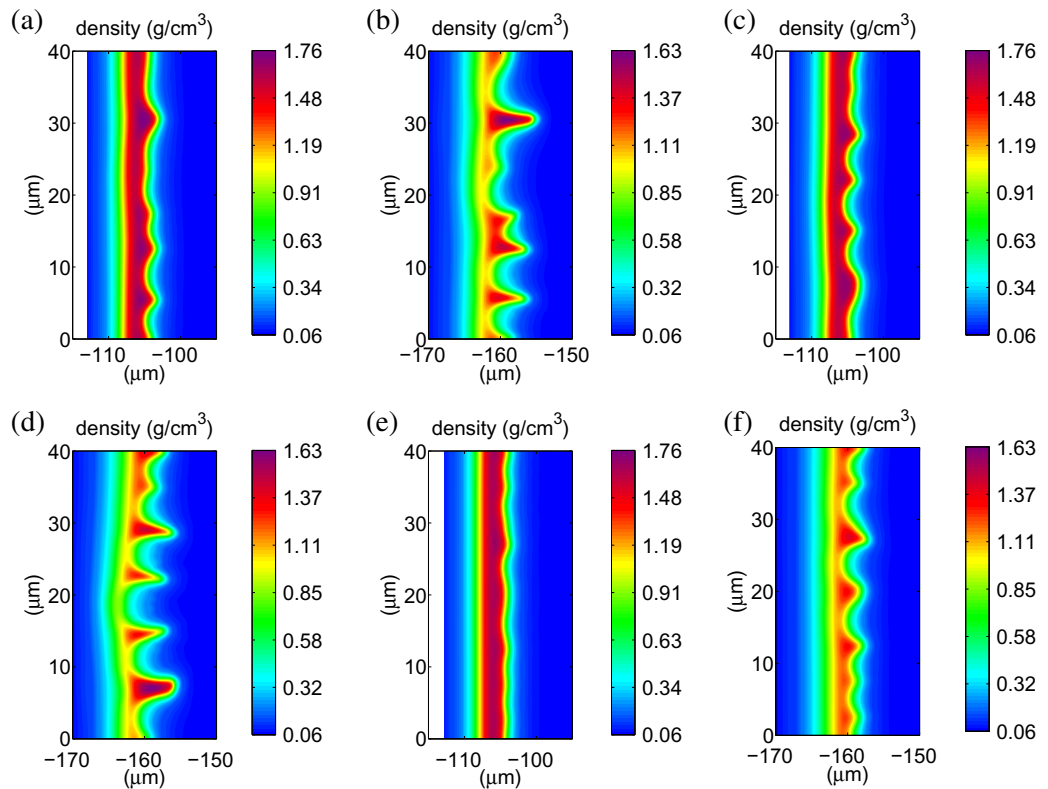


**Figure 9.** Isocontours of the foil density during the acceleration phase for the case of the laser irradiation without foam (a), (b) (large coherence time  $\tau_c$  and  $l_c = 3 \mu\text{m}$ ); for the case of the spatially smoothed laser irradiation (large coherence time  $\tau_c$  and  $l_c = 1 \mu\text{m}$ ) (c), (d); and for the case of the spatially and temporally smoothed laser irradiation (e, f) ( $\tau_c = 1 \text{ ps}$  and  $l_c = 1 \mu\text{m}$ ). The time moments are  $t = 1 \text{ ns}$  (a), (c), (e) and  $1.2 \text{ ns}$  (b), (d), (f).

amplitude is decreased by a factor of two at the same time compared to the two previous cases. Thus, a lower level of the seed increases the time of the linear RT instability development while the growth rate remains unchanged. Certainly, this result is obtained for the same hydrodynamic conditions corresponding to the same target acceleration and the same ablation velocity.

The important result of this paper is that the plasma induced temporal laser beam smoothing makes the dominant contribution to the laser imprint reduction. The density distributions present an instantaneous snapshot of the instability effect on the foil acceleration. A temporal evolution of the areal density perturbation for all three cases is shown in figure 10. One can distinguish three subsequent phases already discussed for the single-mode case in section 4.1. The initial perturbation amplitude of the spatially smoothed beam is smaller but almost of the same order than for the case without foam. In contrast the initial amplitude of the temporally smoothed imprinted perturbation is three to six times lower than for the case without foam during the ablative RM. This difference is then reduced at the beginning of acceleration but there is still a factor of 2 during the RT development. This analysis of the different phases contributing to the final perturbation level is quite general. The smoothing effect may be further enhanced by searching the characteristics of the foil and intensity to control the dominant

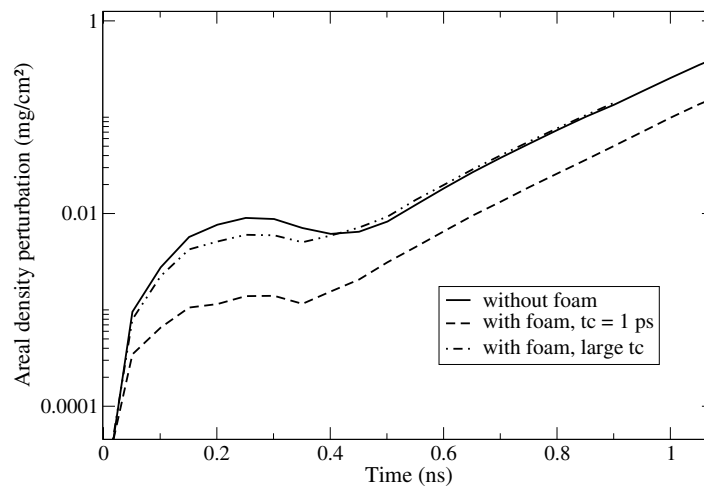


**Figure 10.** Temporal evolution of the areal density perturbation in the foil, for the case without the foam smoothing effect (solid line), for the case of a temporally coherent but spatially smoothed laser beam (dashed-dotted line) and for the temporally and spatially smoothed laser beam (dashed line).

perturbation wavelength of RM and RT phases. For instance, choosing an appropriate relation between the oscillation period of the RM phase and the shock crossing time may be achieved by either adjusting the foil thickness or the wavelength of the most unstable mode.

## 5. Conclusion

The effect of an underdense plasma on the laser imprint reduction and the growth of hydrodynamic instabilities is investigated in a series of multi-dimensional numerical simulations for the set of parameters typical for the ICF target implosion in the direct-drive approach. The hydrodynamic simulations show that the foam is converted into an underdense hot plasma after the ionization wave traverses the foam. As the ionization wave propagates with a supersonic velocity, the laser intensity perturbations are not imprinted at the ionization front, but smoothed out by the complex laser–plasma interaction. Paraxial simulations show that the laser beam propagation through the foam is accompanied by spatial and temporal modifications of the speckle pattern. The intensity distribution spectrum is spread towards smaller wavelengths and the frequency spectrum is broadened. This latter effect corresponds to the reduction of the time-average amplitude of the intensity fluctuations.

Hydrodynamic stability of a plastic (CH) foil placed at the rear side of the foam is studied in 2D single-mode and multimode simulations with the code CHIC. The wavelengths of the fastest growing hydrodynamic modes are three to ten times larger than the laser speckle size. The development of such long wavelength perturbations is rather weakly affected by the spatial effect of plasma induced smoothing. Thus the spatial laser beam smoothing corresponding to broadening of the wavelength spectrum has very little effect on the perturbation level during RT instability growth. This conclusion is rather general and may apply to the typical ICF configuration.

In contrast, the temporal laser beam smoothing related to the frequency spectrum broadening demonstrated a clear mitigation effect. As the characteristic spectral width is larger than the RT instability growth rate, the effective amplitude of the long wavelength perturbations is reduced. This results in a delay in the RT instability evolution. Our simulations show that the imprinted laser intensity perturbation in the foil can be reduced by a factor from 3 to 6 leading to the delay in the ablative RT instability evolution with a reduction by a factor 2 of the perturbation amplitude.

The major foam smoothing effect on the ablative RT instability seeding is thus not in the reduction of the speckle size, but in the reduction of the beam coherence time.

The simulations have been performed for foam densities of 5 and 10 mg cc<sup>-1</sup>. This range of density is limited by hydrodynamic and interaction considerations. A denser foam would reduce the velocity of the supersonic ionization wave. It will be transformed in a shock wave as soon as its velocity becomes subsonic. Moreover, the laser energy absorption increases as the foam density increases. A less dense foam would require unreasonable large thickness in order to enable the smoothing effect. In addition, the lower density foams are too fragile and could not be produced and manipulated with existing technology.

The recent experiment [24] shows that the ionization front velocity is overestimated by a factor of 2 compared to simulations where the foam is replaced by a homogeneous material with equivalent density. This delay corresponds to additional laser energy absorption needed to explode and homogenize the foam structures. Thus, plasma smoothing may be energy consuming for the foam ionization and heating. One has to find a compromise between the benefit from laser beam smoothing and its cost in terms of the laser energy absorption. This fact was not taken into account in the present simulations, where we assumed the same absorbed energy in the foil. In a realistic experimental configuration, the laser intensity incident on the foam needs to be higher in order to compensate the energy losses in the foam. These effects need to be investigated experimentally in order to evaluate the foam efficiency in realistic designs of future ICF targets.

## Acknowledgments

This work was supported by the Aquitaine Regional Council and by the HiPER European project.

## References

- [1] Lindl J 1998 *Inertial Confinement Fusion* (New York: Springer)
- [2] Atzeni S and Meyer-ter-Vehn J 2004 *The Physics of Inertial Fusion* (Oxford: Clarendon)
- [3] Phillips L, Gardner J H, Bodner S E, Colombant D, Obenschain S P, Schmitt A J, Dahlburg J P, Lehecka T, Klapisch M and Bar-Shalom A 1999 *Laser Part. Beams* **17** 225  
Gardner J H, Bodner S E and Dalburg J P 1991 *Phys. Fluids B* **3** 1070
- [4] Betti R, Anderson K, Knauer J P, Collins T J B, McCrory R L, McKenty P W and Skupsky S 2005 *Phys. Plasmas* **12** 042703
- [5] Knauer J P *et al* 2005 *Phys. Plasmas* **12** 056306
- [6] Goncharov V N, Knauer J P, McKenty P W, Radha P B, Sangster T C, Skupsky S, Betti R, McCrory R L and Meyerhofer D D 2003 *Phys. Plasmas* **10** 1906

- [7] Collins T J B and Skupsky S 2002 *Phys. Plasmas* **9** 275  
Collins T J B, Knauer J P, Betti R, Boehly T R, Delettrez J A, Goncharov V N, Meyerhofer D D, McKenty P W, Skupsky S and Town R P J 2004 *Phys. Plasmas* **11** 1569
- [8] Fujioka S *et al* 2004 *Phys. Plasmas* **11** 2814
- [9] Fiksel G *et al* 2012 *Phys. Plasmas* **19** 062704  
Hu S X *et al* 2012 *Phys. Rev. Lett.* **108** 195003
- [10] Sanz J, Betti R, Smalyuk V A, Olazabal-Loumé M, Drean V, Tikhonchuk V T, Ribeyre X and Feugeas J L 2009 *Phys. Plasmas* **16** 082704
- [11] Drean V, Olazabal-Loumé M, Sanz J and Tikhonchuk V T 2010 *Phys. Plasmas* **17** 122701
- [12] Yañez C, Sanz J and Olazabal-Loumé M 2012 *Phys. Plasmas* **19** 062705
- [13] Watt R G *et al* 1997 *Phys. Plasmas* **4** 1379
- [14] Labaune C *et al* 1992 *Phys. Fluids B* **4** 2224
- [15] Schmitt A J and Afeyan B B 1998 *Phys. Plasmas* **5** 503
- [16] Pesme D, Rozmus W, Tikhonchuk V T, Maximov A V, Ourdev I G and Still C H 2000 *Phys. Rev. Lett.* **84** 278
- [17] Michel P, Labaune C, Weber S, Tikhonchuk V T, Bonnaud G, Riazuelo G and Walraet F 2003 *Phys. Plasmas* **10** 3545
- [18] Lushnikov P M and Rose H A 2004 *Phys. Rev. Lett.* **92** 255003
- [19] Grech M, Riazuelo G, Pesme D, Weber S and Tikhonchuk V T 2009 *Phys. Rev. Lett.* **102** 155001
- [20] Malka V, Faure J, Hüller S, Tikhonchuk V T, Weber S and Amiranoff F 2003 *Phys. Rev. Lett.* **90** 075002
- [21] Grech M, Tikhonchuk V, Riazuelo G and Weber S 2006 *Phys. Plasmas* **13** 093104
- [22] Depierreux S *et al* 2009 *Phys. Rev. Lett.* **102** 195005
- [23] Riazuelo G and Bonnaud G 2000 *Phys. Plasmas* **7** 3841
- [24] Nicolai Ph *et al* 2012 *Phys. Plasmas* **19** 113105
- [25] Nicolai Ph *et al* 2011 *Bull. Am. Phys. Soc.* **56** 235
- [26] Goncharov V N 1999 *Phys. Rev. Lett.* **82** 2091
- [27] Piriz A R, Sanz J and Ibañez L F 1997 *Phys. Plasmas* **4** 1117
- [28] Goncharov V N, Skupsky S, Boehly T R, Knauer J P, McKenty P, Smalyuk V A, Town R P J, Gotchev O V, Betti R and Meyerhofer D D 2000 *Phys. Plasmas* **7** 2062
- [29] Maire P-H, Breil J, Abgrall R and Ovadia J 2007 *SIAM J. Sci. Comput.* **29** 1781  
Breil J, Galera S and Maire P-H J 2011 *Comput. Fluids* **46** 161
- [30] Gus'kov S Yu, Limpouch J, Nicolai Ph and Tikhonchuk V T 2011 *Phys. Plasmas* **18** 103114
- [31] Weber S, Maire P-H, Loubère R, Riazuelo G, Michel P, Tikhonchuk V and Ovadia J 2005 *Comput. Phys. Commun.* **168** 141
- [32] Brantov A V, Bychenkov V Yu, Tikhonchuk V T, Rozmus W and Senecha V K 1999 *Phys. Plasmas* **6** 3002
- [33] Kato Y *et al* 1984 *Phys. Rev. Lett.* **53** 1057
- [34] Le Cain A, Riazuelo G and Sajer J M 2011 *Phys. Plasmas* **18** 082711
- [35] Rose H A and Dubois D F 1992 *Phys. Fluids B* **5** 590
- [36] Pesme D *et al* 2002 *Plasma Phys. Control. Fusion* **44** 53
- [37] Feugeas J L, Nicolai Ph, Ribeyre X, Schurtz G, Tikhonchuk V and Grech M 2008 *Phys. Plasmas* **15** 062701
- [38] Betti R, Goncharov V N, McCrory R L and Verdon C P 1998 *Phys. Plasmas* **5** 1446
- [39] Sanz J, Betti R, Ramis R and Ramirez J 2004 *Plasmas Phys. Control. Fusion* **46** B367